Mechanical Stress Evaluation by Neutrons and Synchrotron Radiation

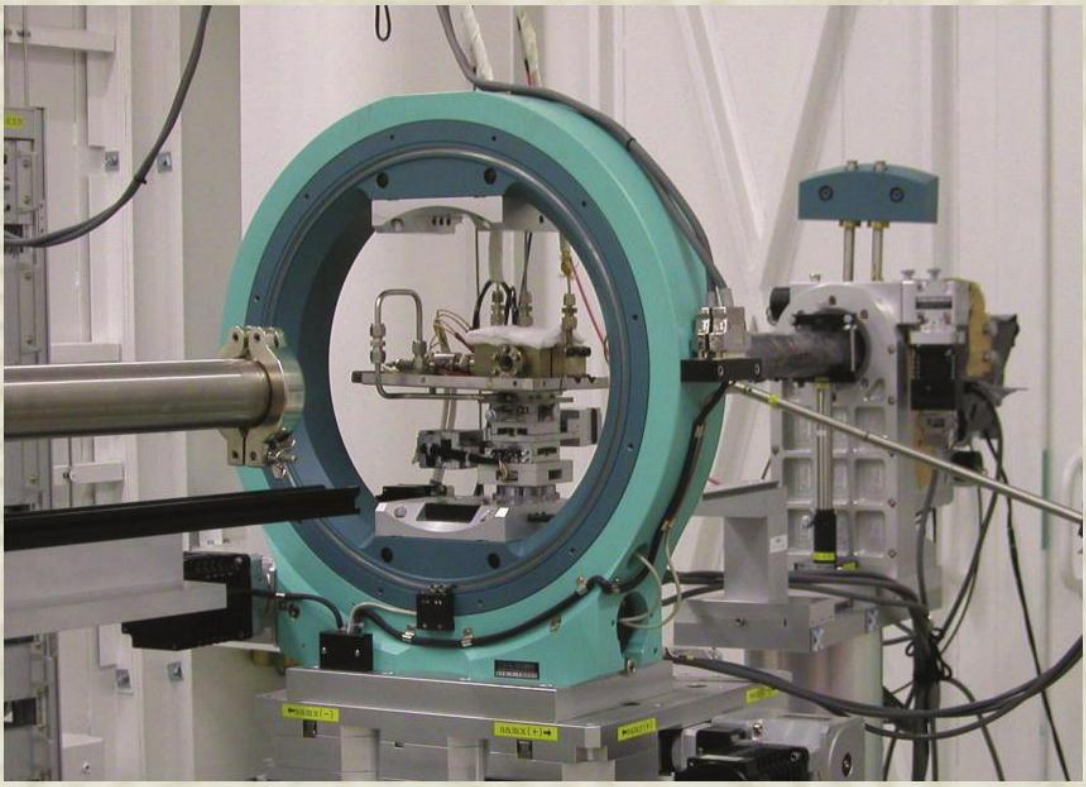

Edited by
Y. Akiniwa, K. Akita and H. Suzuki

TRANS TECH PUBLICATIONS

Mechanical Stress Evaluation by Neutrons and Synchrotron Radiation

Edited by
Y. Akiniwa
K. Akita
H. Suzuki

Mechanical Stress Evaluation by Neutrons and Synchrotron Radiation

Selected, Peer reviewed papers from the MECA SENS V (The 5th International Conference on Mechanical Stress Evaluation by Neutrons and Synchrotron Radiation)/ QuBS2009 (The 3rd International Symposium of Quantum Beam Science Directorate of Japan Atomic Energy Agency), Mito 10 - 12 November 2009

Edited by:

Y. Akiniwa, K. Akita and H. Suzuki

TRANS TECH PUBLICATIONS LTD
Switzerland • UK • USA

Trans Tech Publications Ltd
Laubisrutistr. 24
CH-8712 Stafa-Zurich
Switzerland
http://www.ttp.net

Volume 652 of
Materials Science Forum
ISSN 0255-5476

Full text available online at *http://www.scientific.net*

***Distributed** worldwide by*

Trans Tech Publications Ltd
Laubisrutistr. 24
CH-8712 Stafa-Zurich
Switzerland

Fax: +41 (44) 922 10 33
e-mail: sales@ttp.net

and in the Americas by

Trans Tech Publications Inc.
PO Box 699, May Street
Enfield, NH 03748
USA

Phone: +1 (603) 632-7377
Fax: +1 (603) 632-5611
e-mail: sales-usa@ttp.net

PREFACE

Neutron and synchrotron radiation are novel and powerful tools for stress evaluation and widely applied to fundamental studies in materials science and engineering, and to various industrial fields. MECA SENS V, the 5th International Conference on Mechanical Stress Evaluation by Neutrons and Synchrotron Radiation, was held at Mito, Japan, from November 10th to 12th, 2009, as a joint meeting with QuBS2009, the 3rd International Symposium of Quantum Beam Science Directorate of Japan Atomic Energy Agency, which was sponsored by the Japan Atomic Energy Agency and Ibaraki University. Previous conferences of MECA SENS were at Reims, France in 2000, Manchester, UK in 2003, at Santa Fe, USA in 2005 and Vienna, Austria in 2007. This MECA SENS V was the first conference held in Asia/Oceania. 186 scientists and engineers from the academic world and industry of 20 countries attended this conference with 96 oral presentations in 20 scientific sessions, including 3 keynote lectures, 17 invited lectures, and 51 poster presentations.

The conference brought together scientists from the academic world and industry to address specific topics concerning evaluations of stresses and related phenomena using neutrons, synchrotron radiation and X-rays. Many presentations in stress testing were dealing with samples up to 0.5 m line pipe. Many applications of microbeam X-ray methods were described ranging from intragranular stress fluctuations within a grain ascribed to dislocations to the stresses in interconnects on chips. Simultaneous evaluation of tomography and stress measurements on the same sample was shown to provide extremely clear insights into the nature and cause of damage. A major advance in the simulation of stress and strain on the mesoscopic scale has been achieved in the extended elasto-plastic self-consistent model.

MECA SENS conferences always identify many interesting new studies related to materials science and engineering using neutron and synchrotron radiation. We can witness the evolution of these researches over the years in this collection.

March 30th, 2010

Conference chairs

Yo TOMOTA (Ibaraki University)

Yukio MORII (Hitachinaka Techno Center, QuBS/ JAEA)

This conference "MECA SENS V/ QuBS2009" is

Sponsored by:

Japan Atomic Energy Agency,
Ibaraki University

Co-sponsored by:

High Energy Accelerator Research Organization,
RIKEN,
Japan Synchrotron Radiation Research Institute,
Ibaraki Prefectural Government,
JSMS Committee on X-ray Study on Mechanical Behavior of Materials

Local Committee of MECA SENS V/ QuBS2009

Chairpersons:

Yukio MORII (Hitachinaka Techno Center, QuBS/ JAEA), Yo TOMOTA (Ibaraki University)

Advisory Committee:

M. ARAI (J-PARC Center/ JAEA), D.F. CHEN (CIAE, China),
M. HAYASHI (Ibaraki Prefectural Government), T. KAMIYAMA (J-PARC Center/ KEK),
O. KIRSTEIN (ANSTO, Australia), C.H. LEE (KAERI, Korea),
RIDWAN (BATAN, Indonesia), K. TANAKA (Meijo University), N. UMESAKI (JASRI)

Steering Committee:

Y. AKINIWA (Yokohama National University), K. AKITA (Tokyo City University),
S. HARJO (J-PARC Center/ JAEA), I. HIROSAWA (JASRI), T. ISHIGAKI (Ibaraki University),
H. KONISHI (KPSI/ JAEA), S. NISHINO (Ibaraki University), Y. SAKAIDA (Shizuoka University),
T. SHIRAO (QuBS/ JAEA), T. SHOBU (QuBS/ JAEA), K. SUZUKI (Niigata University),
T. SUZUKI (Ibaraki University), M.TAKAHASHI (Ibaraki Prefectural Government),
Y. TAKANO (Ibaraki Prefectural Government), S. TORII (KENS/ KEK),
M. YONEMURA (Ibaraki University)

Conference Secretary:

Hiroshi SUZUKI (QuBS/ JAEA)

International Scientific Committee

M. BOURKE (USA), D. BROWN (USA), C. BRAHAM (France), T. BURSLAPS (Germany),
H. CHOO (USA), M. DAYMOND (Canada), H.P. DEGISCHER (Austria),
L. EDWARDS (Australia), M. FITZPATRICK (UK), C. GENZEL (Germany),
T. HOLDEN (Canada), A. KRAWWITZ (USA), A. LODINI (France) , P. LUKAS (Czech Rep.),
Y. MORII (Japan), I.C. NOYAN (USA), T. PIRLING (France), A. PYZALLA (Germany),
H.G. PRIESMEYER (Germany), W. REIMERS (Germany), M. RIPLEY (Australia),
R. ROGGE (Canada), A. SCHREYER (Germany), J.-M. SPRAUEL (France),
A. STEUWER (France), H. SUZUKI (Japan), K. TANAKA (Japan), Y. TOMOTA (Japan),
X.-L. WANG (USA), K. WIERZBANOWSKI (Poland), P.J. WITHERS (UK)

Table of Contents

Materials Science Forum Vol. 652 (2010) pp 1-6

doi:10.4028/www.scientific.net/MSF.652.1

Optimization of Material Properties Using Genetic Algorithms

Krzysztof WIERZBANOWSKI[1,a], Jacek TARASIUK[1,b] and Alain LODINI[2,c]

[1] Faculty of Physics and Applied Computer Sciences, AGH University of Science and Technology, al. Mickiewicza 30, 30-059 Kraków, Poland

[2] LACM-DTI, Université de Reims Champagne Ardenne, 9, bd. de la Paix, 51100 Reims, France

[a]wierzbanowski@ftj.agh.edu.pl, [b]tarasiuk@novell.ftj.agh.edu.pl, [c]alain.lodini@univ-reims.fr

Keywords: Genetic algorithms, Crystallographic texture, Elastic constants, Materials optimization

Abstract. The genetic algorithm method was used in the present work as an alternative to classical calculation methods. It can be used in the situations where we search an optimal solution and a problem has many variable parameters. In this work the genetic algorithm method was applied in order to decompose the texture function into ideal components and also to optimize elastic constants by an appropriate choice of texture function. These example applications of genetic algorithm method show its potential in the field of material engineering.

1. Introduction

The genetic algorithms method (GAM) is a modern computer technique widely used in different fields of technique and science. This method was originally based on some ideas taken from biological evolution theory [1,2]. GAM is especially useful for a study of problems, which are not completely determined. They are, e.g., problems having a few but not very different solutions or problems without a strict (exact) solution. GAM can be useful in the latter situation if it is enough to find a good solution but not necessarily the best one. In GAM approach it is not necessary to know a priori a general scheme of problem solution; however, it is important to have a procedure estimating the quality of a solution. This procedure is necessary to eliminate some solutions and to accept another. In last years GAM was used with increasing success in different areas of science, e.g., in: sociology, construction engineering, artificial intelligence and many others.

2 . Genetic algorithm method

The basic elements of GAM will be shortly recalled below. As it was already mentioned, it is not necessary to know a priori a general scheme of solution of a given problem but it is important to have a procedure estimating the quality of a solution. This procedure is called *accommodation function*. Each possible solution I of a studied problem is called an *individual* and is defined as a string of coefficients (*coding procedure*), e.g:
$I\ (\ p_1\ ,\dots\ ,\ p_2\ ,\ p_3,\dots\ ,\ p_M\ )$.

The algorithm starts with an initial random set of solutions: I_1, I_2, ... I_N :

$I_1\ (p_{11}\ ,\dots\ ,\ p_{12}\ ,\ p_{13},\dots\ ,\ p_{1M})$
$I_2\ (p_{21}\ ,\dots\ ,\ p_{22}\ ,\ p_{23},\dots\ ,\ p_{2M})$
……
$I_N\ (p_{N1}\ ,\dots\ ,\ p_{N2}\ ,\ p_{N3},\dots\ ,\ p_{NM})$

The set of solutions is called *population* P. Consecutive iterations are done next; in each iteration three basic numerical operations are performed on solutions: *reproduction, mutation* and *crossover* [1,2].

- During *reproduction* each solution I_n from the population P_k gets some number of copies, proportional to its accommodation factor. The solutions with accommodation factor below a mean value for the population are removed.
- During *crossover* some (randomly chosen) pairs of solutions are retained. Next, some parts of their coefficient strings are cut in the same point and are interchanged. In the example below, the crossover for the solutions I_x and I_y is shown. The parts of coefficient strings (with indices from *1* to *r*) were cut and interchanged.

$I_x (p_{x1} ,\dots , p_{xr} , p_{x(r+1)} ,\dots , p_{xM})$ $\quad\quad$ $I_x (p_{y1} ,\dots , p_{yr} , p_{x(r+1)} ,\dots , p_{xM})$

$I_y (p_{y1} ,\dots , p_{yr} , p_{y(r+1)} ,\dots , p_{yM})$ $\quad\quad$ $I_y (p_{x1} ,\dots , p_{xr} , p_{x(r+1)} ,\dots , p_{yM})$

Solutions I_x and I_y before crossover $\quad\quad$ Solutions I_x and I_y after crossover

- During *mutation* some coefficients in some solutions are randomly changed,

After carrying out these operations on the population, P_k one gets the population P_{k+1} (starting population for the next iteration). The quality of the best solutions increases systematically with the number of iterations (populations). Calculations are stopped when the quality of the best solution is satisfactory.

3. Use of genetic algorithms in texture decomposition

The crystallographic texture is one of basic characteristics of materials. Using texture, it is possible to evaluate a macroscopic property of a material if the same quantity (and its anisotropy) is known at the crystal scale. A strict quantitative representation of texture is given by the orientation distribution function (ODF). This function gives a unique characteristic of the distribution of crystal orientations. On the other hand it enables the calculation of average physical properties for a polycrystalline material.

ODF is generally calculated from a set of experimental pole figures, determined by X-ray or neutron diffraction. There exist a number of methods for this calculation (see e.g., 6-12). Having already determined ODF, it is practical in many cases to present it as a sum of main texture components, i.e., as a sum of Gauss type functions centred on selected ideal orientations. Such the decomposition enables a quick texture analysis or a simplified calculation of a sample property. This decomposition can be done using classical numerical methods (e.g., Minuit algorithm) but the calculation time becomes very long with increasing number of used texture components. Therefore, the method proposed in this work is based on the texture decomposition into Gauss type model functions [13], where their parameters and weight coefficients are found by GAM.

GAM can be also used to find optimal textures for selected material properties. Calculation of elastic constants (EC) or diffraction elastic constants (DEC) is a good example of ODF application to find macroscopic properties from crystalline ones. These constants are used in the interpretation of internal stress measurements by diffraction techniques. Two elements are necessary to calculate EC or DEC: elastic constants of single crystal (S_{ijkl} or C_{ijkl}) and numerical values of ODF. Generally, ODF is represented by its values in a set of points (forming a regular grid) in the Euler space. Each point in the Euler space defines the crystal orientation g with respect to the sample reference frame and it is expressed by φ_1, ϕ, φ_2 angles [6]. Hence, the crystal orientation can be characterized directly by three Euler angles $g = \{\varphi_1, \phi, \varphi_2\}$ or by the orientation matrix g calculated using these angles [6]. In the most frequent case of cubic crystal symmetry and orthorhombic sample symmetry, φ_1, ϕ, φ_2 vary in $[0^o, 90^o]$ range, and $\Delta\varphi_1=\Delta\phi=\Delta\varphi_2=5^o$ steps are used for

discretization; consequently ODF is presented by 19*19*19=6859 values. Stocking a huge amount of ODFs can create the computer memory problems. This difficulty is avoided if ODF is decomposed into Gauss peaks (typically of the order of ten); only a few parameters have to be recorded to define a peak (location, width and volume). This provides a tool of simplified (but sufficient for many practical purposes) texture analysis. Another advantage coming from the proposed analysis is the possibility of simplified DECs calculation using only a few texture components (ideal orientations). In this approach a property of the textured material can be approached as an average property for a few single crystals with different orientations.

The basic idea of the proposed ODF representation is to express it as a sum of Gauss-shaped functions. Special standard functions, adapted to texture analysis, defined by Matthies [13], were used:

$$f(S,\varpi) = N(S)\exp(S\cos\varpi) \tag{1}$$

where $\varpi = \varpi(g_o, g)$ is the angular distance between the orientations g_o and g (g_o is the orientation of the peak centre and g is any orientation; $0 \le \varpi \le \pi$) and S is the parameter connected with the peak width: $S=\ln 2/[2\sin^2(b/4)]$ with $b \le 2\pi$. The factor N(S) is the normalization constant ($N(S)=[I_o(S)-I_1(S)]^{-1}$, where I_k are modified Bessel functions [13]); it may be shown that for reasonably narrow Gauss-shaped functions ($\varpi << \pi$), an approximated formula can be used: $N(S) \approx e^{-S}\sqrt{8\pi S^3}$. Each standard function is normalized:

$$\int_G f(S,\varpi)dg = 8\pi^2 \tag{2}$$

where G denotes the orientation space. Let us note that each standard function is defined by b and g_0. Our goal is to decompose an ODF (we denote it as F(g)) into a sum of standard functions:

$$F(g) = \sum_{m=1}^{M} a_m f_m(b_m, g_{0(m)}) \tag{3}$$

where M is the total number of used standard functions and a_m are weight coefficients ($0 \le a_m \le 1$). The standard functions are normalized (Eq.2), hence the weight coefficients give also the volume fractions of grains whose orientations are covered by a given standard function. Each standard function, with its weight coefficient a_m, is located at a specific orientation $g_{0(m)}$ (in texture nomenclature it is called an ideal orientation) and is defined by the half-width b_m, which in turn defines its S_m parameter.

The condition which has to be fulfilled during optimisation (accommodation function) is that the sum of considered standard functions has to be as close as possible to the analysed ODF (χ^2 test is used). Each solution (I_n) contains the share coefficients (a_m), widths (b_m) and three Euler angles defining the centres of the Gauss functions: $g_{0(m)} = g_0(\varphi_{1(m)}, \Phi_m, \varphi_{2(m)})$:

$$I_n(a_1, b_1, \varphi_{1(1)}, \Phi_1, \varphi_{2(1)}, a_2, b_2, \varphi_{1(2)}, \Phi_2, \varphi_{2(2)}, \ldots\ldots, a_M, b_M, \varphi_{1(M)}, \Phi_M, \varphi_{2(M)}) \tag{4}$$

The example result of texture decomposition using this type of individuals is shown in Fig 1. The experimental texture function (Fig. 1a) was decomposed into sum of five standard functions (Eq. 3) and this sum is presented in Fig. 1b.

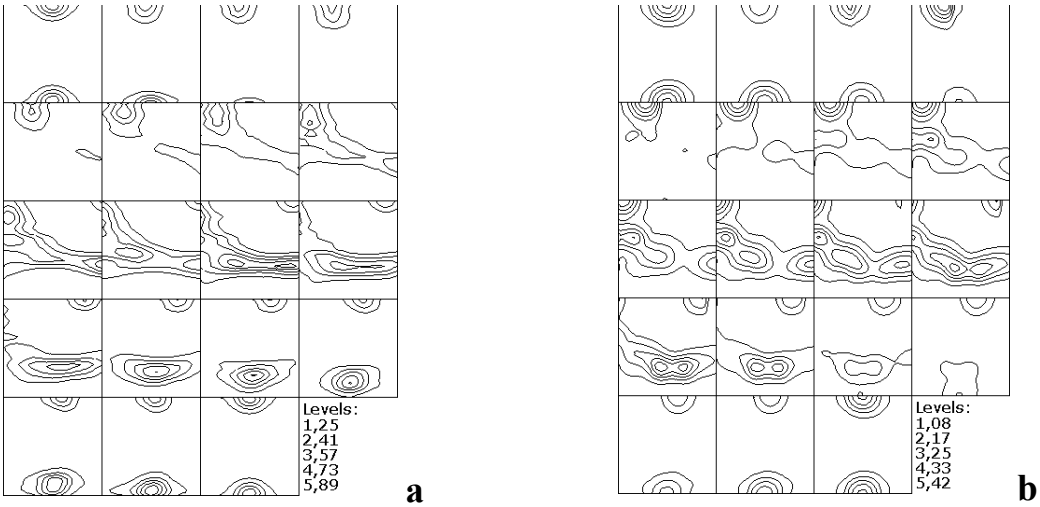

Fig. 1. Reproduction of the cold rolled steel texture: a) experimental texture, b) texture reproduced by GAM using individuals (Eq. 4) containing M=5 standard functions. φ_2=const sections are shown.

The convergence of calculations, i.e. the variation of the accommodation factor vs. the number of generations is shown in Fig. 2. We note that GAM procedure is quickly convergent and after approximately hundred generations one obtains a satisfactory solution. It should be noted that in the case of M=5 used standard functions, GAM is 3-4 times faster than the classical Minuit algorithm. Moreover, this difference grows rapidly (in favor of GAM) with increasing number of Gauss standard functions.

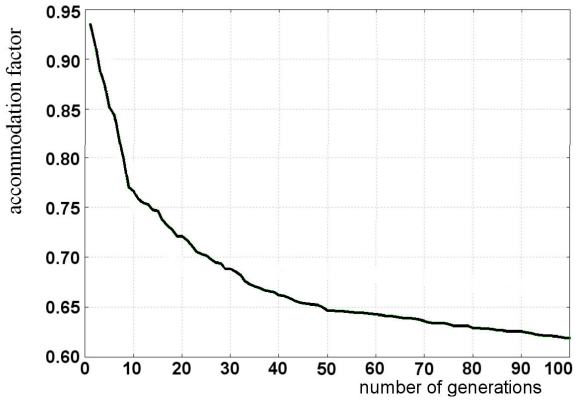

Fig. 2. Accommodation factor vs. number of generations

4. Optimization of macroscopic elastic constants

Another application of GAM, considered in this work, concerns the research of optimal elastic constants of a material. Elastic properties of crystal are described by two tensors: S_{ijkl} (compliance) and C_{ijkl} (stiffness) [14]. Calculation of the macroscopic average (i.e., sample property) will be presented for S_{ijkl} tensor. It involves two steps. In the first one the single crystal tensor S_{mnop} is transformed to the sample co-ordinates system:

$$S_{ijkl}'(g) = g^{T}_{im} g^{T}_{jn} g^{T}_{ko} g^{T}_{lp} S_{mnop} \tag{5}$$

where g if the orientation matrix defining the crystal lattice orientation of a grain, generally expressed by three Euler angles: φ_1, ϕ, φ_2. This matrix relates the sample reference frame $\mathbf{K_A}$ to the crystal one $\mathbf{K_B}$, i.e.: $\mathbf{K_B}$=g $\mathbf{K_A}$, and g^T is the transposed matrix of g. Moreover, the standard repeated index summation convention is applied in Eqs. 5 and 6. In the second step the transformed elastic tensor ($S_{ijkl}'(g)$) is averaged next to obtain the mean macroscopic tensor S^M_{ijkl}'. The texture function, F(g), is the weighting parameter [6]:

$$S^M_{ijkl}' = \int_\Omega S_{ijkl}'(g)\,F(g)\,dg = \int_\Omega g^T_{im} g^T_{jn} g^T_{ko} g^T_{lp} S_{mnop}\,F(g)dg \tag{6}$$

and Ω is the basic volume of the Euler angles space. An optimal texture is often searched to produce a material with required properties. Let us perform a simple test of the presented method. The proposed example is to find a texture, which assures a minimal Young's modulus (E) of the material along the $\mathbf{x_1}$ sample axis. This condition imposes the maximum value of $S^M_{11}'=S^M_{1111}'$ (because $E=1/S^M_{1111}'$).

Three independent constants (S_{11}, S_{12}, S_{44}) define elastic properties of cubic crystals [14] (standard matrix notation S_{nm} will be used for S_{ijkl} in the following text). The tensor transformation from crystal co-ordinates system to the sample one gives:

$$S^M_{11}' = S_{11} + \{S_{44} - 2(S_{11} - S_{12})\}(g^{T\,2}_{11} g^{T\,2}_{12} + g^{T\,2}_{12} g^{T\,2}_{13} + g^{T\,2}_{13} g^{T\,2}_{11}) \tag{7}$$

The following S_{ij} values for low carbon steel were used in the calculations:
S_{11}=7,5682·10^{-6} MPa^{-1}, S_{12}= -2.78·10^{-6} MPa^{-1} and S_{44}= 8,5911·10^{-6} MPa^{-1} [15].
Hence Eq.7, after substituting the above constants, takes form (S^M_{11}' is expressed in MPa):

$$S^M_{11}' = 7.5682 - 12.1053(g^{T\,2}_{11} g^{T\,2}_{12} + g^{T\,2}_{12} g^{T\,2}_{13} + g^{T\,2}_{13} g^{T\,2}_{11}) \tag{8}$$

The calculation of optimal elastic properties was done using the formula for texture function given by Eq. 3 (with M=5). The orthorhombic sample symmetry and cubic crystal symmetry were taken into account in the calculations.

The texture (ODF), leading to a minimal Young's modulus (i.e., maximal S^M_{11}'value) , found by GAM is shown in Fig. 3a; it is composed of the cube texture component (001)[100] (i.e., φ_1=0^0, ϕ=45^0, φ_2=45^0). The same procedure was used to find a texture leading to the maximal Young's modulus (Fig. 3b) and it contains two components: the $(110)[1\bar{1}\bar{1}]$ (i.e., φ_1=35^0, ϕ=90^0, φ_2=45^0 and approximately the $(112)[\bar{1}\bar{1}1]$ (i.e., φ_1=90^0, ϕ=35^0, φ_2=45^0) one.

Let us perform a quick analytical test of the above results. A minimal value of Young's modulus corresponds to a maximal value of S^M_{11}', and according to Eq. 8, it is reached for a *zero value* of the following factor:

$$X = g^{T\,2}_{11} g^{T\,2}_{12} + g^{T\,2}_{12} g^{T\,2}_{13} + g^{T\,2}_{13} g^{T\,2}_{11} \tag{9}$$

This is verified for {hkl}<100> texture components. And in fact, the texture found by GAM contains the cube component: (001)[100] (for which X=0). Similarly, a maximal value of Young's modulus is reached for the maximal value of X=1/3. This condition is verified for {hkl}<111> components and, indeed, our GAM calculated texture contains $(112)[\bar{1}\bar{1}1]$ and $(110)[1\bar{1}\bar{1}]$ ones. The above examples confirm that GAM procedure works correctly.

a **b**

Fig. 3. Textures found by GAM leading to: a) minimal Young's modulus, b) maximal Young's modulus (b). $\varphi_2=45^0$ section is shown.

6. Conclusions

GAM can be used to find material parameters which lead to optimal properties. It furnishes good results (but not necessarily the best one) verifying some imposed criteria. In each practical case a reasonable compromise between the calculation time and the solution quality has to be found. In the present work the test example of optimisation concerns the Young's modulus, but the method is quite general and it can be applied to other physical properties.

Acknowledgements

This work was supported by the Polish Ministry of Science and Education (MNiSW) and by EU Network of Excellence: "Complex Metallic Alloys" (CMA).

References:

[1] J.H. Holland, Adaptation in natural and artificial systems, The University of Michigan Press, USA (1975)
[2] D.E. Goldberg, Genetic Algorithms in Search, Optimisation and Machine Learning, Addison- Wesley Publishing (1989)
[3] P. Sałek, J. Tarasiuk and K. Wierzbanowski, Cryst. Res. Technol., Vol. 34 (1999) p. 1073
[4] P. Sałek, J. Tarasiuk, K. Wierzbanowski, Arch. of Metall., Vol. 44 (1999) p. 175
[5] J. Tarasiuk, K. Wierzbanowski and B. Bacroix, Comp. Mater. Sci. Vol. 29, (2004) p. 179
[6] H. J. Bunge, Texture Analysis in Materials Science, Butterworths, London (1982)
[7] K. Lücke, J. Pospiech and J. Jura, Zeit. Metallk., **77,** 312 (1986)
[8] H. Schaeben, H.: Phys. stat. sol. (b), Vol. 148 (1988) p. 63
[9] D. Ruer and R. Baro, Adv. X-ray Anal., Vol. 20 (1977) p. 187
[10] S. Matthies, Phys. stat. sol., Vol. B92 (1979) p. K135
[11] K. Pawlik, Phys. stat. sol. (b), Vol. 134 (1986) p. 477
[12] J. Tarasiuk, K. Wierzbanowski and A. Baczmański, Cryst. Res. Technol.,Vol. 33 (1998) p. 101
[13] S. Matthies, G.W. Vinel and K. Helming, Standard Distributions in Texture Analysis, Akademie - Verlag, Berlin (1987)
[14] J. F. Nye, Physical Properties of Crystals, Their Representation by Tensors and Matrices, Oxford, Clarendon Press (1957)
[15] G. Simoms, H.Wang, Single Crystal Elastic Constants and Calculated Aggregate Properties: A Handbook, The M.I.T. Press, Cambridge, Massachusetts, London (1971)

Materials Science Forum Vol. 652 (2010) pp 7-12

doi:10.4028/www.scientific.net/MSF.652.7

Residual Microstress of Austenitic Stainless Steel due to Tensile Deformation

Kenji Suzuki [1,a] and Takahisa Shobu [2,b]

[1] Department of Technology, Faculty of Education, Niigata University, Igarashi-2-no-cho, Nishi-ku, Niigata, 950-2181, Japan

[2] Advanced Beamline Development Group, Japan Atomic Energy Agency, Koto, Sayo, Hyogo, 679-5148, Japan

[a] suzuki@ed.niigata-u.ac.jp, [b] shobu@sp8sun.spring8.or.jp

Keywords: Austenitic stainless steel, Plastic deformation, Residual microstress, Elastic anisotropy, Syn- chrotron X-ray, Intergranular strain

Abstract. Material of the specimen was austenitic stainless steel (SUS316L). The specimens were given tensile plastic strains from 0% to 55%. The Vickers hardness of the specimen corresponded to the plastic strain. The residual macrostress was measured by Mn-*K*α radiations. The residual macrostress of the annealed specimen had a small compression and changed into a tension after tensile plastic deformation. The specimen with 1% plastic strain showed the maximum tensile residual stress. To examine the dependency of the residual stress on the lattice plane, the residual microstress for each lattice plane was measured by hard synchrotron X-rays. The residual microstress was related with Young's modulus which was calculated by Kröner model. A new method, 2θ-$\cos^2\chi$ method, was proposed to solve the problem of coarse grains and it was excellent in comparison with the $\sin^2\psi$ method.

Introduction

Hereafter, nuclear power plants in Japan are going to exceed 40 years from operations. A study on stress corrosion cracking (SCC) is indispensable as a measure against the nuclear plant aging. The austenitic stainless steel has large elastic anisotropy. Plastic deformation induces the residual microstress into the stainless steel, because plastic deformation depends on a lattice plane. We have to investigate the behavior of the residual microstress due to plastic deformation.

The study on elastic-plastic anisotropic deformation of the austenitic stainless steel was performed using a neutron diffraction method. Each lattice spacing was measured under uniform tension, its mechanical behavior was compared with a self consistent model [1,2]. The residual strains were measured from 200, 220, 311, 222 diffractions and the plastic deformation for each step was observed by TEM [3]. As for a current research, the main object was the relation between the applied stress and the elastic strain.

The residual stress due to plastic deformation is the fundamentals of SCC. In this study, the main object was put on the residual stress due to plastic deformation. The residual stresses in the austenitic stainless steels with some kinds of plastic strains were measured using many diffraction planes and the dependency of the residual microstress on the lattice plane was discussed.

Experimental Methods

Specimen and Plastic Strain. The material used in this study was austenitic stainless steel (SUS316L). The sizes of the plate specimen were a thickness of 3 mm, a width of 15 mm and a length of 55 mm. In order to release the residual strain after machining, the specimens were annealed at 913 K for 10

min. The proof stress was 202 MPa and the tensile strength was 523 MPa. The mean grain size of the specimen was 55 μm.

The specimens were deformed with a tensile testing machine. The cross-head speed was 0.2 mm/min (strain rate: 6.06×10^{-5} /s). The plastic strain of each specimen was measured after unloading. Although the prescribed plastic strains were 0, 0.2, 1, 2, 5, 10, 20 and 55%, the actual plastic strains were 0, 0.23, 0.99, 2.13, 4.98, 9.25, 19.0 and 54.8 %.

Measurement of Residual Stress. The residual macrostresses were measured using a 2θ-$\sin^2\psi$ method before and after the plastic deformation. The γ-Fe 311 diffraction by Mn-$K\alpha$ radiation was used in consideration of high accuracy and efficiency.

To examine the dependency of the residual microstress on the lattice plane, the stress has to be measured using a lot of lattice planes. Therefore, the residual stresses were measured by hard synchrotron X-rays. The experiment was made on the beamline BL02B1 at SPring-8. The used X-ray energy was 71.79 keV, the sizes of the divergent and receiving double slits were 0.2×2 mm^2.

Because the irradiated area and the divergent angle of the synchrotron beam are small, the problem due to coarse grains appears. To solve the problem, the followings were discussed; 1) a transmission method with hard synchrotron X-rays, 2) an oscillation method with a rotation, 3) a method without a strain-free lattice spacing, d_0. As a new method, the 2θ-$\cos^2\chi$ method is proposed. This is a kind of the $\sin^2\psi$ method of a transmission type.

The ψ is the angle between the normal direction to the diffraction plane and specimen surface. The χ angle is the complementary angle of ψ and equal to $\pi/2 - \psi$ as shown in Fig. 1. When a diffraction angle is small, the incident X-ray beam can penetrate into the specimen. The axis of the measuring stress, $\overline{OX}$, is tilted χ against the normal to the diffraction plane. When the stress, σ_x, is a uniaxial stress state, the relation between the diffraction angle, $2\theta_\chi$ and χ is given by

$$2\theta_\chi - 2\theta_0 = -\frac{2(1+\nu)}{E}\tan\theta_0 \cdot \sigma_x \cos^2\chi + \frac{2}{E}\tan\theta_0 \cdot \sigma_x \qquad (1)$$

where θ_0 is the diffraction angle for the strain-free material, E and ν are X-ray elastic constants. The stress, σ_x, is calculated from a slope of the 2θ-$\cos^2\chi$ diagram. The advantage of the $\cos^2\chi$ method is as follows; 1) The value of $\cos^2\chi$ can change from 0 to 1 because of a transmission method. 2) The specimen with coarse grains can be rotated around the stress axis in a uniaxial stress state. 3) The irradiated area in the specimen surface can be kept constant with the change in the χ angle.

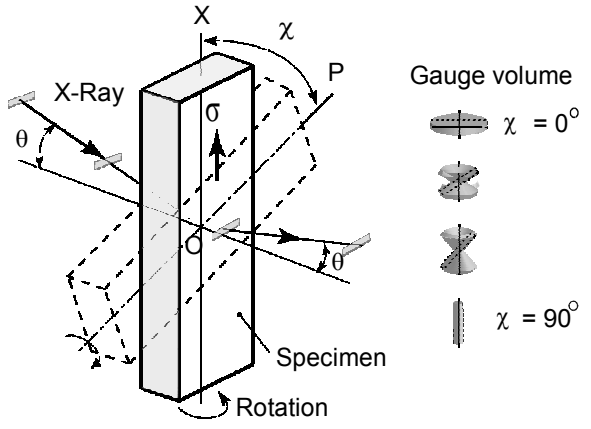

Fig. 1. 2θ-$\cos^2\chi$ method with rotation.

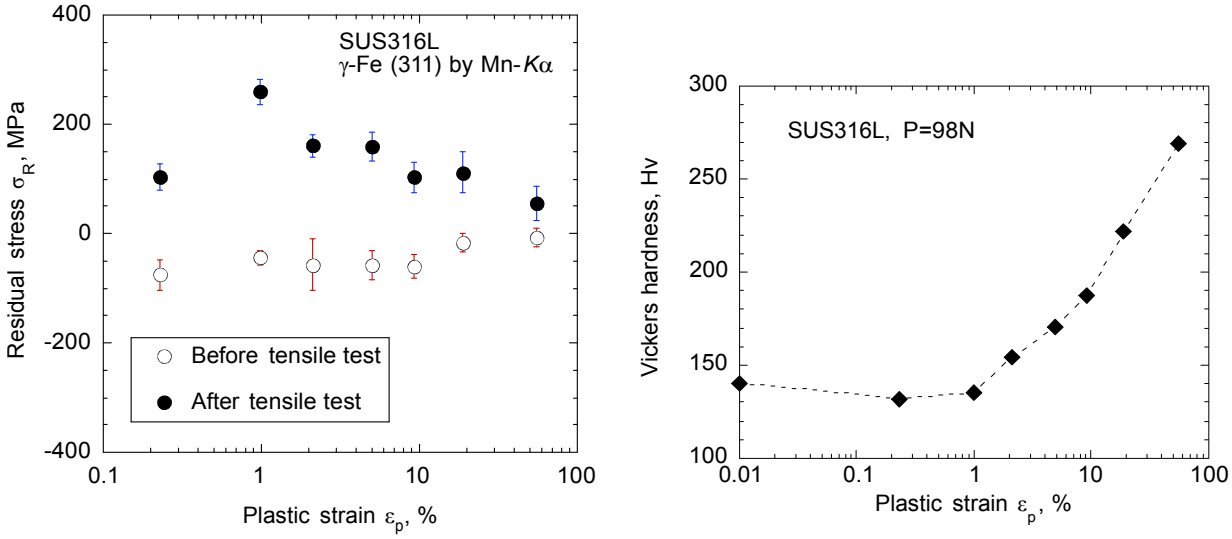

(a) Residual stress (b) Vickers hardness

Fig. 2. Changes in residual stress and hardness with increase in plastic strain.

The X-ray elastic constants used in this study were calculated by Kröner model [4]. The values of the stiffness for SUS316 single crystal are $c_{11} = 206$, $c_{12} = 133$ and $c_{44} = 119$ GPa quoted from another paper [5]. The web system was prepared to calculate the elastic constants of arbitrary lattice plane (hkl) by Kröner model [6].

Results and Discussion

Change in Residual Stress and Hardness. The change in the residual stress before and after plastic deformation is shown in Fig. 2 (a). The error bar in the figure indicates the confidence limit of 68.3%. The residual stress of each specimen was a small compression before the plastic deformation and changed a tension after the plastic deformation. The specimen with a few percentage plastic strains showed a large residual stress against other specimens. An intergranular strain is introduced due to the plastic anisotropy exceeding the yield stress [7]. For the large plastic strain, the effect of the intergranular strain becomes small due to the large deformation and preferred orientation.

Figure 2 (b) shows the change in Vickers hardness with the increase in plastic strain. As the abscissa in Figs. 2 are a logarithmic axis, the plastic strain of $\varepsilon_p = 0$ is plotted at the position of 0.01 for the sake of convenience. Vickers hardness keeps constant in the plastic strain of 1% or less. However, Vickers hardness changes correspond to plastic strain more than 2%.

2θ-$\cos^2\chi$ Method. Figure 3 (a) shows the 2θ-$\sin^2\psi$ diagram and the peak height is demonstrated in addition to 2θ in the figure. The relation between 2θ and $\sin^2\psi$ is not good as shown in the Fig. 3 (a), because the peak height is small due to the preferred orientation in 0.4 or more $\sin^2\psi$. On the other hand, the 2θ-$\cos^2\chi$ diagram is shown in Fig. 3 (b). The peak height near the value of 0.5 is higher than that by the $\sin^2\psi$ method. The relation between 2θ and $\cos^2\chi$ has a good agreement as shown in Fig. 3 (b). As a result, the $\cos^2\chi$ method with rotation is useful for the stress measurement of the specimen with coarse grains.

Residual Microstress due to Plastic Deformation. The specimens were given the prescribed plastic strains by a uniaxial tension then unloaded. The residual microstress for each lattice plane was measured by the $\cos^2\chi$ method with hard synchrotron X-rays.

For the specimens with the plastic strain of 1 and 2 %, the residual microstress for each lattice

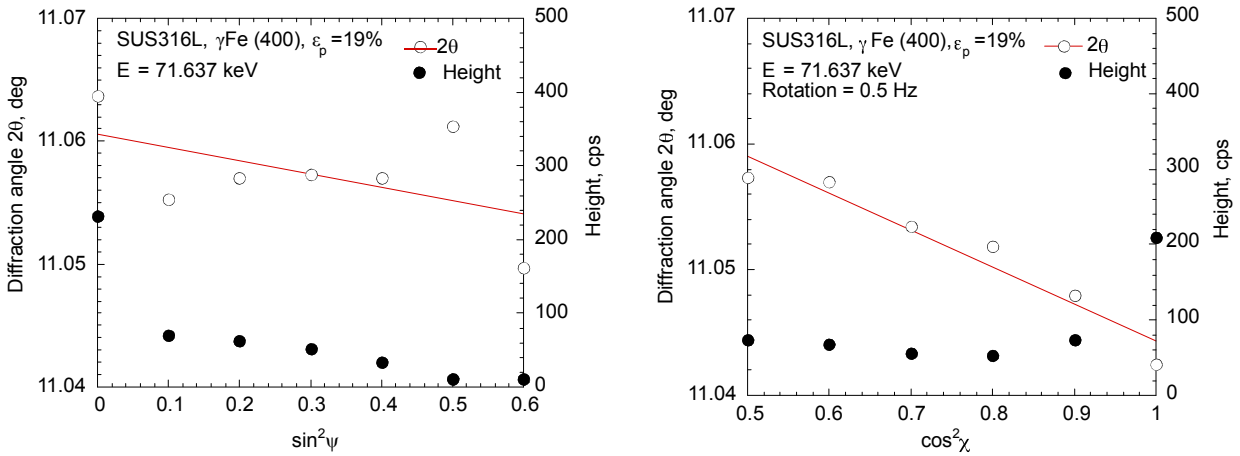

(a) $\sin^2\psi$ method (b) $\cos^2\chi$ method with rotaion

Fig. 3. Comparison between $\sin^2\psi$ and $\cos^2\chi$ methods.

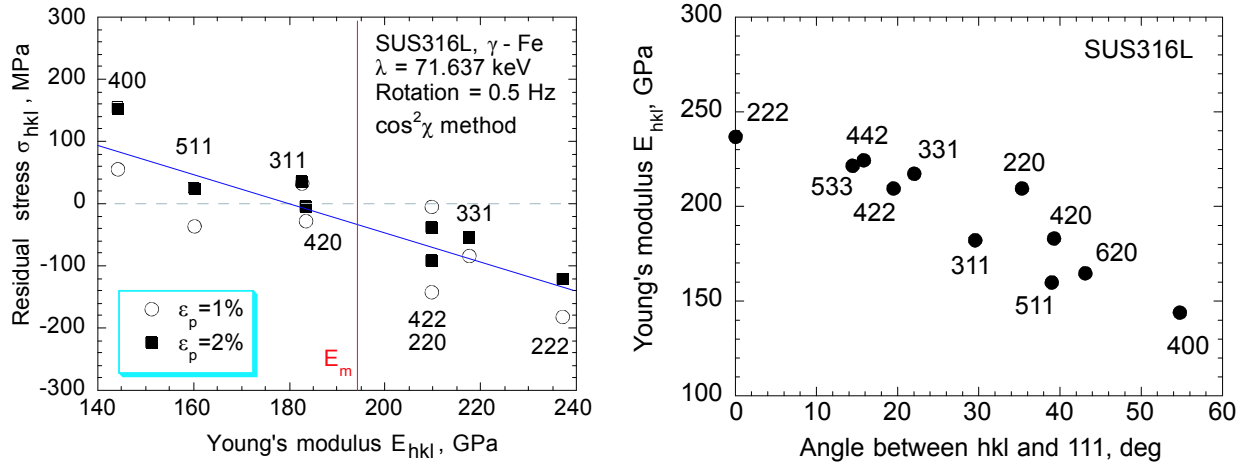

(a) Residual microstresses (b) Angle between *hkl* and 111 plane

Fig. 4. Relation between residual microstresses and Young's moduli by Kröner model.

plane *h k l* is shown in Fig. 4 (a). In the figure, the residual microstress is related with Young's modulus by Kröner model, the solid straight line is the regression line and E_m indicates the mechanical Young's modulus. The residual microstress, σ_{hkl}, is distributed from a tension to a compression, though the residual macrostress idoes not exist because of unloading. For the lower Young's modulus, the residual microstress becomes a tension and the lattice plane for the higher Young's modulus shows a compressive residual microstress. The residual microstress for each plane is called the second kind of residual stress [8]. The residual microstresses are balanced each other. The Young's modulus of the 3 1 1 diffraction is close to the mechanical value and the residual microstress becomes small as shown in Fig. 4 (a). The residual microstress relates to Young's modulus by Kröner model.

In Fig. 4 (b), Young's moduli for *h k l* are plotted against the angle between the 111 and *h k l* planes. The 111 plane is a slip plane of a fcc crystal system, the shearing stress becomes a maximum at 45° to the tensile direction. The elastic anisotropy reflects the direction of the slip plane as shown in the figure. The residual microstress is related with the Young's modulus, and the elastic anisotropy of Young's modulus is related with the direction of the slip plane.

Figure 5 shows the elastic curved surface. The elastic constant, E_{hkl}, is calculated by Kröner

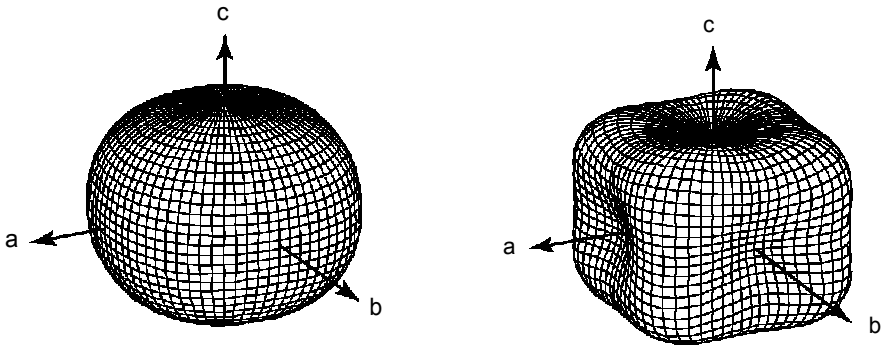

(a) Al (b) SUS316

Fig. 5. Elastic curved surface.

model, the radius and direction are composed of E_{hkl} and [$h\,k\,l$], where the radius is normalized by the mechanical Young's modulus, E_m. As shown in Fig. 5 (a), the elastic curved surface for aluminum is close to a sphere and aluminum behaves like an isotropic material. The austenitic stainless steel has the same fcc crystal system as aluminum. However, the elastic curved surface for SUS316 is different from that for aluminum, and SUS316 has a large elastic anisotropy as shown in Fig. 5 (b).

The elastic anisotropic parameter for cubic system, A, is defined as follows [9];

$$A = \frac{2c_{44}}{c_{11} - c_{12}} \tag{2}$$

where c_{ij} is the stiffness of a single crystal. Concretely calculating, aluminum has A =1.23 [10] and SUS316 has A = 3.26 [5]. The austenitic stainless steel SUS316 has a large elastic anisotropy. The grain with the hard lattice plane is difficult to be deformed from the viewpoint on the elastic and slipping deformation. On the other hand, the grain with the soft lattice plane is easy to be deformed.

Figure 6 shows the mechanism of inducing the residual microstress due to plastic deformation. The strain measured by the X-ray corresponds to the lattice strain. The residual microstress is not induced within an elastic deformation as shown in Fig. 6 (a). Figure 6 (b) demonstrates the behavior of each grain near the yield strain. The intergranular slipping begins around the hard grain, so the lattice strain of the hard grain does not increase. The soft grain is deformed easily because of a law Young's modulus and slipping deformation. The Young's modulus in the soft grain appears to decrease due to

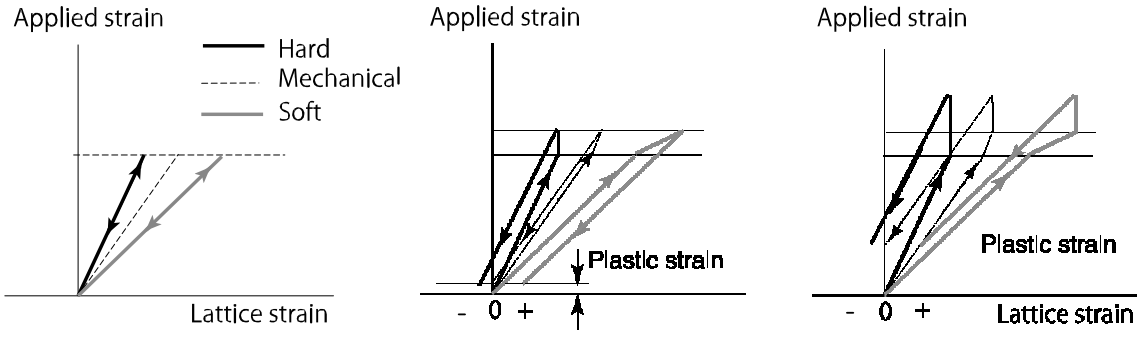

(a) Elastic strain (b) Small plastic strain (c) Large plastic strain

Fig. 6. Inducing residual microstress with tensile plastic deformation.

undertaking the applied stress of the hard grain. The unloading process stops where the mechanical strain is 0. As a result, the hard grain and the soft grain have a compression and a tension, respectively.

For the large plastic deformation in Fig. 6 (c), the soft grain is also deformed plastically. In unloading, each strain returns according to the same mechanism as Fig. 6 (b). In the large scale yielding, the residual microstress does not increase, even if the plastic deformation increases as shown in Fig.6 (c). Therefore, the residual microstress is induced in the beginning of the plastic deformation.

Conclusions

The residual microstresses of SUS316L were measured using many lattice planes after the tensile plastic deformation. The main results obtained are as follows:
(1) The residual microstress of each lattice plane can be measured by the $\cos^2\chi$ method with rotation. The $\cos^2\chi$ method is useful for the stress measurement of a material with coarse grains as compared with the $\sin^2\psi$ method.
(2) The residual microstress due to the tensile plastic deformation is dependent on the lattice plane and is related with Young's modulus calculated by Kröner model.
(3) The plastic strain of each grain is not uniform in the beginning of yielding because of elastic anisotropy. After unloading, the inhomogeneous plastic strain causes the residual microstress.
(4) Vickers hardness corresponds to the plastic strain in the range of more than 2% plastic strains.

Acknowledgment

The authors acknowledge financial support of a grant in aid for science research from the Ministry of Education, Culture, Sports, Science and Technology of Japan (No. 21560081). The synchrotron radiation experiments were performed at SPring-8 with approval of the Japan Synchrotron Radiation Research Institute (No. 2007A1108, 2007B1646).

References

[1] B. Clausen, T. Lorentzen and T. Leffers: Acta Metalludica, Vol. 46 (1998), p. 3087.

[2] B. Clausen, T. Lorentzen, M.A.M. Brourke and M.R. Daymond: Material Science & Engineering, A259 (1999), p. 17.

[3] R. Lin Peng, M. Ddén, Y.D. Wang and S. Johansson: Material Science & Engineering, A334 (2002), p. 215.

[4] E. Kröner: Zeiteschrift Physik, Vol. 151 (1958), p. 504.

[5] H.M. Ledbetter: British Journal of NDT, Vol. 23 (1981), p. 286.

[6] http://x-ray.ed.niigata-u.ac.jp/xdatabase/Kroner_model/kroner_c.html

[7] T.M. Holden: J. Neutron Research, Vol. 7 (1999), p. 291.

[8] K. Tanaka, K. Suzuki and Y. Akiniwa, *Evaluation of Residual Stresses by X-Ray Diffraction — Fundamentals and Applications*, p. 187, Yokendou (2006).

[9] *Ibid.* at p. 257.

[10] G.N. Kamm and G.A. Alers: Journal of Physics and Chemistry of Solids, Vol. 35 (1964), p. 327.

Materials Science Forum Vol. 652 (2010) pp 13-18

doi:10.4028/www.scientific.net/MSF.652.13

Intergranular Strains in Pre-Strained and Welded Pipes

M. O. Acar[1, a], P. J. Bouchard[2, b], J. Quinta da Fonseca[3, c], M. E. Fitzpatrick[4, d] and S. Gungor[5,e]

[1,2,4,5] Materials Engineering, The Open University, Walton Hall, Milton Keynes MK7 6AA, UK

[3] Manchester Materials Science Centre, Grosvenor St, Manchester M1 7HS, UK

[a]m.o.acar@open.ac.uk, [b]p.j.bouchard@open.ac.uk, [c]joao.fonseca@manchester.ac.uk, [d]m.e.fitzpatrick@open.ac.uk, [e]s.gungor@open.ac.uk

Keywords: Neutron diffraction, Weld residual stresses, Intergranular residual strains, Plastic deformation

Abstract. Neutron diffraction has been used to investigate the weld residual stresses and the intergranular residual strains in butt-welded 316H pipes. Measurements have been made on pipes subjected to varying degrees of plastic pre-straining before welding, in order to assess the effects of plastic strain on the weld residual stresses and the intergranular strains in the material. The intergranular strains following plastic deformation will also be affected by the annealing effect of the welding. Pipes were initially prepared with plastic strain of 0, 10, 15, 20 and 25% plastic deformation. Thereafter, the pipes were cut in half and welded with a circumferential butt-weld. Bar specimens were extracted from the remote end of the 0, 10, 15, 20 and 25% pre-strained and welded pipes. Cross-weld bar specimens were also machined from the 0 and 20% pre-strained and welded pipes. Neutron diffraction measurements were made at ENGIN-X, ISIS and FRM-II, Munich.

The aim of this paper is to evaluate the intergranular strains developed after pre-straining from measurements made in remote bar specimens from the remote-end of the pipes. The annealing effect of the welding cycle on the intergranular strains is also studied, with measurements done at several points on cross-weld bar specimens, obtaining the strain response of different *hkl* lattice planes. The results show that the {200} and {220} planes are at the extremes of response during loading. Furthermore, the welding thermal cycling relaxed the intergranular strains from the prior plastic deformation.

Introduction

In many power plants, energy is transferred to the power generator turbines *via* heat exchanger units which are exposed to high temperatures and pressures. Heat exchanger units are manufactured using many metres of austenitic stainless steel tubes which are plastically deformed (swaged or bent) and welded into complex shapes. These fabrication processes alter the mechanical properties of the steel. The introduction of plastic strain increases the susceptibility of the tubing to stress corrosion cracking, creep damage and influences the fracture properties [1]. It also produces significant residual stresses as well as changing yielding properties by work-hardening. Welding introduces residual stresses as a result of the complex thermal-mechanical cycling and varying mechanical properties across the weldment [2]. Finally, post-weld heat treatment is applied to relieve the residual stresses generated by the forming and welding processes, but it may also trigger mechanisms such as recrystallization and precipitation. For the safe operation of power plant, the lifetime of the heat exchangers needs to be predicted. This requires understanding of separate and combined effects of each process on the material properties.

The aim of the work reported here is to investigate the residual strains/stresses developed in stainless steel tubing after plastic pre-straining and welding processes by using neutron diffraction. During plastic forming processes grains begin to deform by the activation of favorably oriented slip systems as the material approaches the macroscopic yield point and this generates a new distribution of strain inside and between the grains. When the forming load is removed, elastic strains develop to balance this localized plastic deformation; these are generally referred to as

residual ‘intergranular strains’ or ‘micro-strains’ and can be determined by neutron diffraction [3]. The effect of subsequent welding is to subject base material to intense thermo-mechanical deformation cycles. This not only introduces macro-residual stresses into the fabricated structure but is also likely to influence the state of the base material including the distribution of intergranular strains associated with prior plastic deformation as well as the microstructure. This paper presents results of neutron diffraction studies measuring macroscopic residual stresses at the Stress-Spec instrument (FRMII, Germany) using the (311) diffraction plane and intergranular strains for different (hkl) planes at the ENGIN-X time-of-flight instrument at the ISIS spallation neutron source, UK.

Test Specimens

A set of five plastically pre-strained and welded tubes were supplied by British Energy, UK. The parent material was AISI Type 316H austenitic stainless steel with composition 16.89 wt% Cr, 11.25 wt% Ni, 2.04 wt% Mo, 1.55 wt% Mn, 0.53 wt% Si, 0.089 wt% Co, 0.05 wt% C, less than 0.05% of other elements and the balance being Fe. The grain size of the material was about 30 μm. The 1% proof strength of the non-strained material was 367 MPa and Young’s modulus for this type of material is about 195 GPa. The tubing (prior to plastic straining) was approximately 38 mm in diameter and 4 mm in thickness. The tubes were first deformed uniaxially up to 0, 10, 15, 20 and 25% total strain in order to simulate plastic deformation associated with fabrication processes in a controlled way. This “pre-straining” process was done using a strain rate of ~0.15%/s with a large servo-hydraulic rig. The pipes were then cut in half and the halves were root tack welded to each other. The welds were completed with the pipe fixed in the vertical position. During the root pass the tacks were incorporated into the weld.

The 0 and 20% pre-strained pipes were used to measure the weld residual stresses (macro-stresses) at Stress-Spec. Thereafter, in order to relax the macro-stresses developed after the pre-straining and welding, and to be able to probe only intergranular strains, remote-end bars were cut from the ends of all five pipes and cross-weld bars were machined out from 0 and 20% pipes by electro-discharge machining (EDM) (Fig. 1). Ten remote-end and eight cross-weld bars were extracted from each tube. The remote-end and cross-weld bars are 75 mm and 107 mm in length respectively. The thickness is 3 mm and the width is 6 mm. These specimens were used for the neutron diffraction experiment at ENGIN-X to investigate the intergranular strains. .

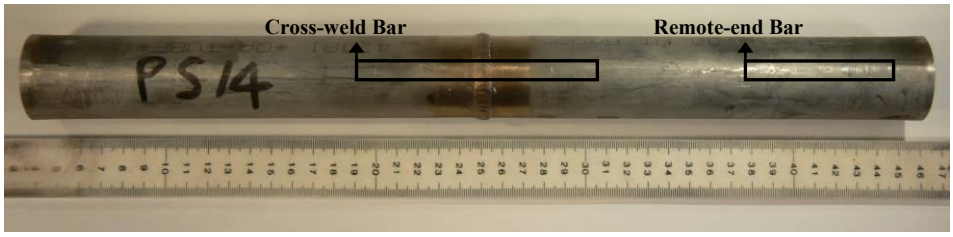

Fig. 1. The position of the cross-weld and remote-end bars from the 20% pre-strained pipe

The crystallographic texture was measured by electron back-scattered diffraction (EBSD) on the coupons extracted from the 0% pipe. It was found that there is 3× random texture for the (111) plane in the axial direction of the pipe.

Neutron Diffraction Experiment at Stress-Spec

The aim of this experiment was to determine the distribution of the weld residual stresses in 0 and 20% pre-strained pipes. A wavelength of $\lambda = 1.5480$ Å was obtained from a Si (400) monochromator. This wavelength allowed measurement of the austenitic steel (311) reflection at a scattering angle of about $2\theta_S \sim 91°$. The gauge volume used in our measurements was $2 \times 2 \times 2$ mm^3. For both tubes, the lattice strain response ε_{lat} in the axial, hoop and radial directions was measured at the mid-thickness along one half of the tubes with a position opposite to the start/stop point of the weld as shown in Fig 2.

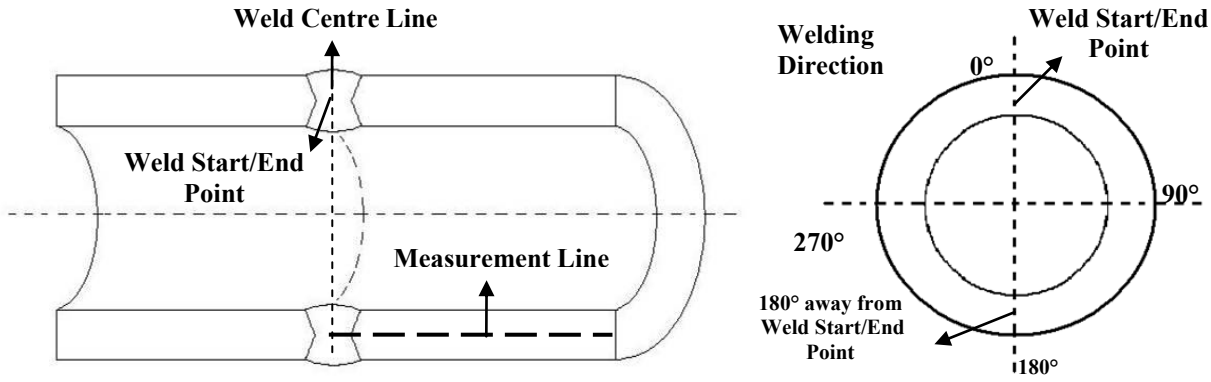

Fig. 2. Schematic of the measurement lines and their positions

The experimental data was analyzed with StressTexCalculator software using Gaussian fitting to obtain the peak positions in terms of 2θ angles which are then used to calculate the strain. Measurements at the remote end of the 0%-tube in axial, hoop and radial directions were used as direction-dependent references (θ_0) to calculate the lattice strain for each measurement.

$$\varepsilon_{lat} = \frac{\Delta d}{d} = \frac{\sin\theta_0}{\sin\theta} - 1 \tag{1}$$

The strain measured is in the direction of the scattering vector. To find out the stress state at any point in the sample, measurements are usually required in six orientations due to the fact that stress is a tensor. However, it was assumed that the principal stress axes coincide with the axial, hoop and radial directions of the tube. Hence the stresses can be calculated with Eq. 2. [4]

$$\sigma_{axial} = \frac{E}{(1+\nu)(1-2\nu)}\left[(1-\nu)\varepsilon_{axial} + \nu\left(\varepsilon_{hoop} + \varepsilon_{radial}\right)\right] \tag{2}$$

where E =195 GPa and ν =0.29.

Neutron Diffraction Experiment at ENGIN-X

The lattice strain response of the material was measured parallel and perpendicular to the pre-straining direction and at some angles between these orthogonal directions by using the data from the two collimator banks at ENGIN-X which provide data for different scattering vectors. ISIS provides a white beam of neutrons to create time-of-flight diffraction patterns. At ENGIN-X the range of the wavelengths in the beam is 0.5-6Å, which means that the data is available from a range of *d*-spacings. First four peaks in the diffraction pattern were selected. To obtain the *d*-spacing of individual peaks a single peak fitting routine implemented in OpenGenie [5] was used. The measurements were performed in the mid-length of the remote-end bars to determine intergranular strains for 0, 10, 15, 20 and 25% pre-straining conditions. The cross-weld bars from 0 and 20% pipes were used to determine the change in intergranular strains due to welding by measuring at the weld centre, and 7, 9, 12, 16 and 29 mm away from weld centre line (Fig. 3). Since the thickness of the bars is small, two adjacent bars were glued together at the outer surfaces with respect to the pipe geometry in order to average as many grains as possible by using a 3 × 3 × 5 mm^3 gauge volume. Neutron currents of 20 μamps were used per measurement, to ensure good peak width signal. The positions of the two adjacent cross-weld bars were opposite to the weld start/end point and close to the macro-residual stress measurement line. The axial and transverse measurements at the mid-length of the 0% pre-strain remote-end bar were used to provide direction-specific references (d_0) to calculate the intergranular strains at the other measurement points on both types of bar. The strain is calculated by using Eq. 3.

$$\varepsilon_{lat}^{hkl} = \frac{d^{hkl} - d_0^{hkl}}{d_0^{hkl}} \tag{3}$$

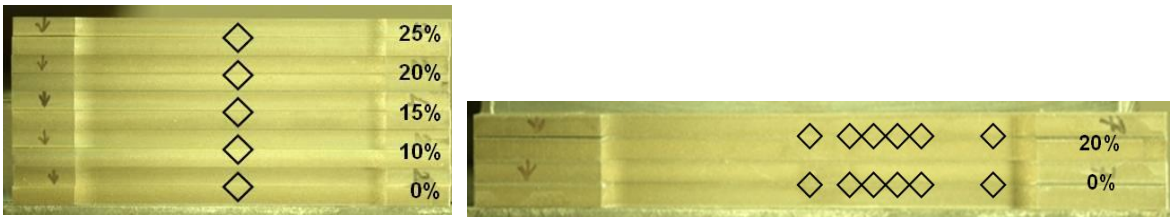

Fig. 3. The remote-end (left) and cross-weld (right) bars and measurement points

Results and Discussion

Macro-residual stresses. Comparing the stress/strain distributions in the remote ends of the tubes (Fig. 4) it is clear that pre-straining has introduced intergranular strains. For both tubes, the welding has affected the stress distribution in the region up to 30mm from weld centre line. In that region it seems that the stress distribution in the undeformed pipe is shifted down in the pre-strained pipe and the axial and hoop stresses are almost doubled in the prestrained pipe. The difference between the strain distributions in that region can be ascribed to the variation in the intergranular strains which were altered by annealing during welding.

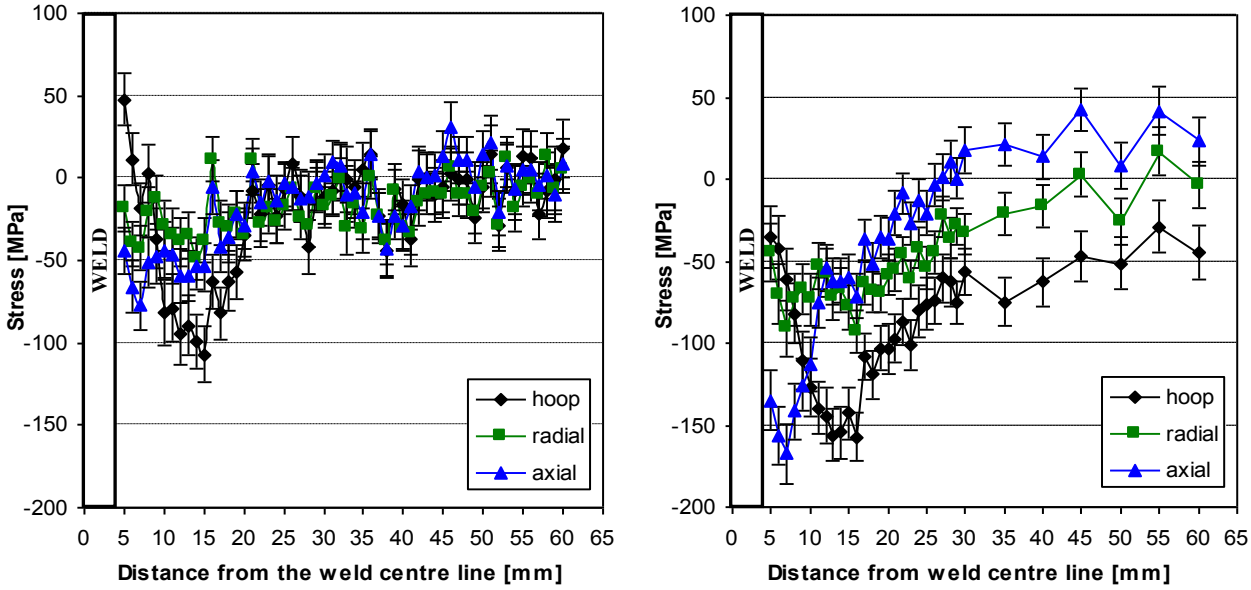

Fig. 4. Residual stress distribution in the 0% (left) and 20% (right) pre-strained pipes on the measurement line obtained from the (311) diffraction plane

Intergranular (micro-) strains. Pang *et al*. showed, by obtaining the Young's modulus of each diffraction plane from modeling and experimental results, that the 111 and 220 grains are stiffer than the 200 and 311 grains [6]. Our results show that the 200 and 311 planes accumulate tensile strains whereas the 111 and 220 planes sustain compressive strains after unloading from different amounts of pre-straining, as can be seen in Fig. 5(c). The change in residual intergranular strains after welding is shown in Fig. 5(a). The measurements on the undeformed welded sample suggest that welding increases the strain in the 220 grains, reaching a minimum at 9 mm and increasing to 0 at 29 mm. Overall, welding appears to reduce the residual elastic strains in the 20% cross-weld bar, particularly in the region closest to the weld. In the prestrained weld, it is again the 220 reflection that shows the biggest change. Near the weld, the 220 strains are tensile, reaching 500 με at 9 mm from the weld line (Fig. 5(b)). Then, it reverses dramatically reaching 1000 με at 16 mm. This

behavior suggests that plastic deformation occurs near the weld during welding. The tensile 220 strains could then be a result of constrained plastic deformation near the weld. The missing point in Fig. 5(b) is due to the less reflection of 220.

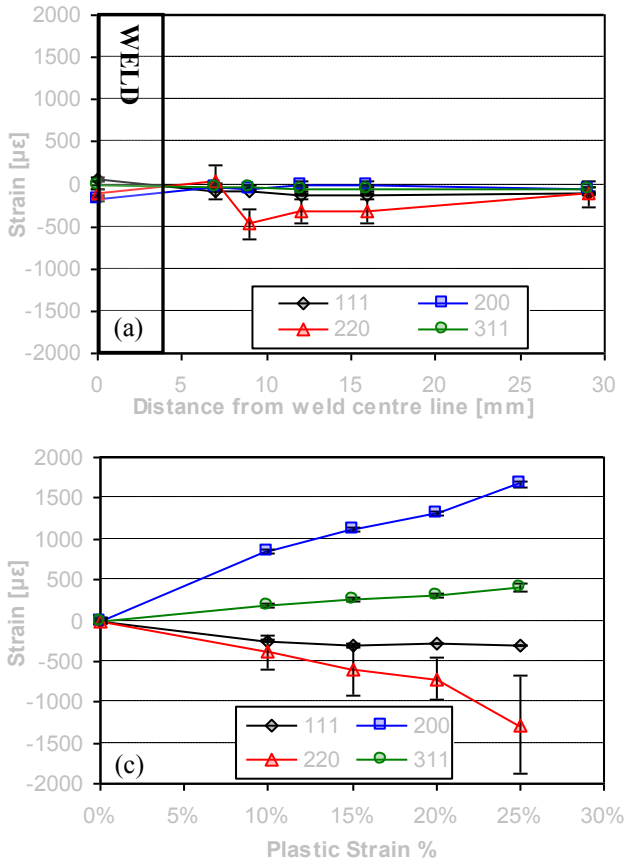

Fig. 5. (a)-(b) Residual intergranular strains in the axial direction for 0% and 20% cross-weld bars, respectively. (c) Development of residual intergranular strains in the axial direction after pre-straining + unloading.

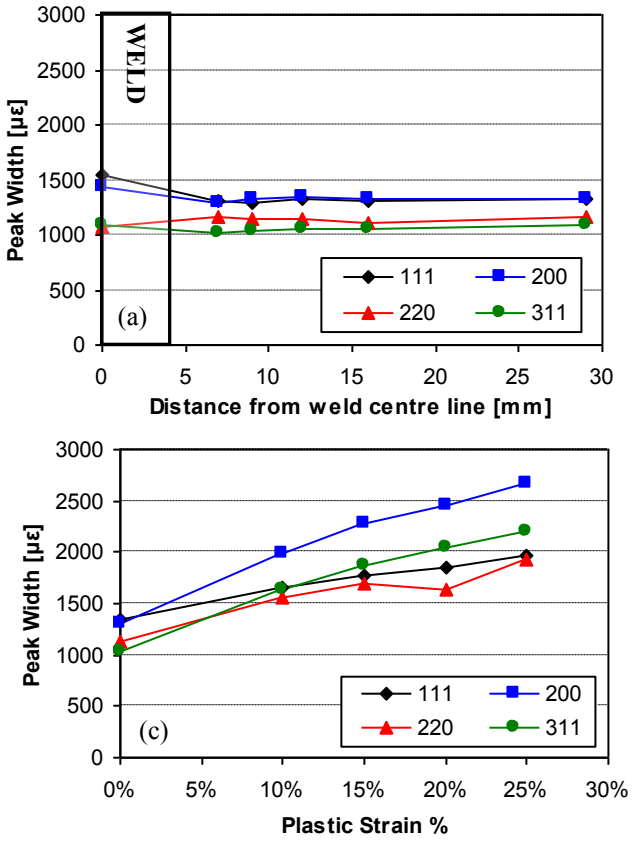

Fig. 6. (a)-(b) Peak widths in the axial direction for the 0% and 20% pre-strained cross-weld bars, respectively. (c) Variation of peak width in the axial direction after pre-straining and unloading.

Peak Widths. The peak width at half maximum data in diffraction patterns are worth to be studied because it enables to compare the dislocation densities and mosaicity qualitatively [7]. In the data shown in Fig. 6, the most reliable data belongs to the strongest peak (111) with a scatter of $0\text{-}50x10^{-6}$. Like the 111 reflection, all peaks show an increase in peak width with increases in plastic deformation. This increase is largest for the 200 reflection and smallest for the 111 (Fig. 6(c)). This is consistent with an increase in dislocation density with increasing plastic strain. In the undeformed welded samples, the peak widths are essentially unchanged by the welding process (Fig. 6(a)). However, in the prestrained specimens, it is clear that the welding reduces the peak width near the weld; at 7mm from weld centre line the width of the 111 peak is the same in the undeformed and prestrained welds (Fig 6(a) and (b)). This implies that the welding has annealed the deformed material in the region near the weld. Slightly further away from the weld, at 9 and 12 mm, the peak widths in the prestrained sample are higher than those in the undeformed weld but lower than those in the far field (29 mm). This is consistent with the weld-induced plastic deformation which had been indicated by the anomalous 220 tensile strains observed in Fig. 5(b).

Conclusions

1. The stresses in the prestrained material are 50% higher than those in the undeformed pipes especially for the axial and hoop components.

2. The internal strains increase with amount of plastic deformation, with 200 and 220 bounding the behaviour for uniaxial deformation.

3. The peak width measurements indicate that, near the weld line, the material is annealed completely.

4. At 9mm, however the peak broadening is already significant. This has two possible causes: incomplete anneal or deformation of the annealed material on cooling.

5. The response of (220) plane near weld varies with the existing plastic deformation. This can be attributed to the recrystallization which was accelerated with the stored energy in the strained material.

Acknowledgements

MOA is funded by British Energy and Dr M. Spindler is thanked for his support. We are grateful for the provision of beam-time at the STFC ISIS facility in the UK and at the FRM-II facility in Munich, and Dr A. Paradowska and Dr M. Hofmann are thanked for experimental support. MEF is supported by a grant through The Open University from the Lloyd's Register Educational Trust (LRET), an independent charity working to achieve advances in transportation, science, engineering and technology education, training and research worldwide for the benefit of all.

References

[1] Kamaya, M., A.J. Wilkinson, and J.M. Titchmarsh, Acta Materialia, 2006. 54(2): p. 539-548.

[2] Chang, K.-H. and C.-H. Lee, Materials and Structures, 2009. 42(6): p. 791-801.

[3] Hauk, V., *Structural and Residual Stress Analysis by Nondestructive Methods* 1997: Elsevier. 59,129.

[4] Hofmann, M. and R.C. Wimpory, Int. J. Pressure Vessels and Piping, 2009. 86(1): p. 122-125.

[5] S. I. Campbell, F. A. Akeroyd, C. M. Moreton-Smith, *Open GENIE - Analysis and Control,* Condensed Matter, arXiv:cond-mat/0210442v2, 2002.

[6] Pang, J.W.L., et al., Acta Materialia, 2000. 48(5): p. 1131-1140.

[7] Quinta da Fonseca, J., et al., Materials Science and Engineering: A, 2006. 437(1): p. 26-32.

Materials Science Forum Vol. 652 (2010) pp 19-24

doi:10.4028/www.scientific.net/MSF.652.19

Synchrotron Strain Mapping Of The Residual Strain Distribution Around Foreign Object Damage In Laser Shock Peened Ti-6AL-4V Alloy

S. Zabeen[1a], M. Preuss[1b], P.J. Withers[1c], S. Spanrad[2d], J. Tong[2e], J. Schofield[3f]

[1.] School of Materials, University of Manchester, Grosvenor St, Manchester M1 7HS, UK

[2.] Mechanical & Design Engineering, Department of Mechanical and Design Engineering, Anglesea Building, Anglesea Road, University of Portsmouth, Portsmouth, PO1 3DJ, UK

[3] Rolls-Royce plc, PO Box 31, Derby, DE24 8BJ, UK

[a]Suraiya.Zabeen@postgrad.manchester.ac.uk, [b]Michael.Preuss@manchester.ac.uk,

[c]Philip.Withers@manchester.ac.uk,

[d]Sven.Spanrad@port.ac.uk, [e]Jie.Tong@port.ac.uk, [f]john.schofield@rolls-royce.com

Keywords: Laser Shock Peening (LSP), Ti-6Al-4V, residual stress, foreign object damage (FOD), LCF/HCF.

Abstract. The current study investigates the effect of foreign object damage (FOD) on the pre-existing compressive residual stress field associated with laser shock peening (LSP) and its evolution upon combined LCF/HCF cycling. FOD was introduced onto an aerofoil-shaped specimen that had been previously LSP treated through ballistic impacts at angles of 0° and 45° to the leading edge. It is shown that the FOD notch created by 45° impact was asymmetric in shape and smaller in depth compared to that created at 0° impact. Significant through thickness compression was introduced parallel to the leading edge as a result of the LSP process. The residual strain distribution was mapped around the FOD notch by synchrotron X-ray radiation. The results show predominantly compressive stresses ahead of the notch, being greater for the 0° compared to 45° impact. No significant stress relaxation was observed after a combined (1000 HCF cycles superimposed on 1 LCF cycle) cycle.

Introduction

Compressor blades are subject to foreign object damage (FOD) that occurs due to the ingestion of hard particles during aircraft take-off, taxiing and landing. Such damage can significantly reduce low, high and combined (both high and low) cycle fatigue strength of aero engine compressor blades. The interplay of several factors is important when considering the effect of FOD on fatigue life: (a) The distribution of residual stress generated by the impact; (b) the stress concentration arising from the FOD geometry; (c) the possibility of microcracks introduced by the impact and (d) the introduction of microstructural damage such as shear banding or local texturing [1]. With respect to (b), a crack growth inhibiting layer of compressive residual stress (CRS) has been shown to be a good way of improving fatigue tolerance to notches in many situations [2]. To introduce a CRS layer, various mechanical surface treatment technologies have been investigated. Laser shock peening (LSP) has been proven to be particularly effective in enhancing the fatigue life of deep notched samples compared to shot peening [3]. In this context it is important to characterise the

residual stress distribution after LSP treatment and its redistribution upon FOD impact. Fatigue testing of in-service turbine blades suggests that damage created at an angle of 45° results in the maximum fatigue strength reduction, hence in this study 45° impacts are studied along with the 0° condition. The aim of this paper was firstly to quantify the level of residual stresses introduced by full-on impact (0°) and impact at 45°, and secondly to determine the extent to which these stresses are modified by fatigue under combined LCF+HCF cycles.

Material and Experimental Method

Material and Specimen. The material studied is Ti-6Al-4V, which is currently used for compressor blades. The manufacturing process involves forging above the β transus of the material, then in the α+β phase field to produce a bimodal microstructure comprising ~60% of primary α and 40% (by volume) of lamellar colonies of α + β. The alloy was then solution treated at about 927°C before stress relief at 705°C for 2 hours. Finally, the samples were machined from the forged blocks. The specimen geometry has been designed to simulate a generic leading edge (Fig 1). The specimens were subsequently laser shock peened over the leading edge using parameters that were optimised so as to maximise the induced CRS, whilst not introducing unacceptable levels of distortion. The extent of the laser shock peened area is 6 mm in width from the edge and 66 mm in length.

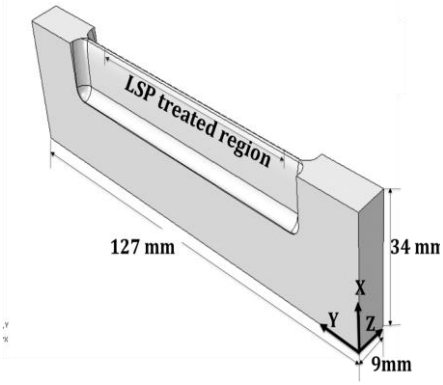

Figure 1: Laser shock peened specimen geometry.

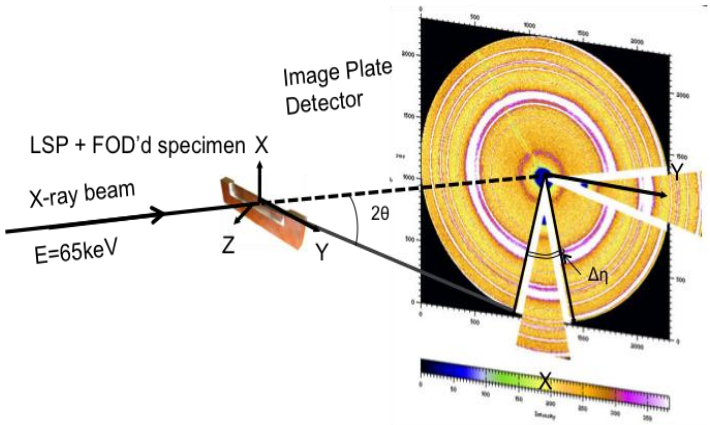

Figure 2: Schematic representation of the experimental setup with an example of the Debye Scherrer ring.

Simulation of FOD. Foreign object damage was simulated by using a compressed gas gun at the Department of Engineering Science, Oxford University to fire the edge of 3 mm hardened steel cubes towards the leading edge of the samples, at angles of 0° and 45° at speeds of 196 m/s and 245 m/s, respectively.

Fatigue testing. The fatigue testing was conducted on a servo-hydraulic twin-actuator 100kN fatigue testing machine designed for high cycle (HCF) and low cycle (LCF) load applications. Experiments were carried out at room temperature under block loading of combined LCF and HCF cycles with 1000 HCF cycles superimposed upon 1 LCF cycle, representing a simplified flight spectrum. The crack growth was monitored using a direct current

potential drop (DCPD) system with nano-voltmeters. The crack lengths were verified post testing from the fracture surfaces. Full experimental procedures may be found in [4].

High Energy Synchrotron X-ray Diffraction. Residual elastic strains were mapped around the FOD damage on the 1-ID-C beamline at APS, ANL, Chicago, USA. A monochromatic synchrotron X-ray beam was used (65keV, 0.1907Å), which enabled measurements to be carried out in through thickness transmission geometry, Fig 2. The diffraction cones were captured on a MAR-345 image plate detector. Therefore it was possible to determine peak shifts and consequently strains in both the directions parallel and perpendicular to the leading edge. Because of the scale of the FOD notches a high spatial resolution was required to accurately measure the strain variation in their vicinity. Therefore, a step-size of 0.2 mm and 0.1 mm was used in parallel and perpendicular to the leading respectively. A gauge volume of $0.1 \times 0.2 \times 2\,\text{mm}^3$ was adequate to capture a sufficient number of diffracting grains resulting in relatively smooth diffraction rings. For each specimen, about 900 individual measurement points (as marked on the maps were collected). Strains were computed from the shift of the $(10\bar{1}2)$ diffraction peak from Ti-α phase. This peak was suitable for elastic strain calculation as it exhibits low intergranular stress development during plasticity. Data analysis was performed by combining FIT2D software and a MATLAB fitting routine. For strain calculation the strain free lattice spacing, d_0 was measured at a location far away from the LSP treated region.

Results and Discussion

Residual Strain Maps. The through thickness averaged strain profile arising from the LSP treatment is shown in Figure 3 both parallel and perpendicular to the leading edge (LE). The plot suggests that the strain component parallel to the leading edge shows a maximum compressive strain of -3500×10^{-6} at the L.E. that gradually decreases with increasing distance from the L.E., becoming tensile at a distance of 6 mm (this corresponds well with the 6mm LSP treated area). In the untreated region it is slightly tensile and diminishes to zero at a distance of 30 mm from the L.E. The shape of the strain profile is broadly consistent with the work done by Frankel [5].

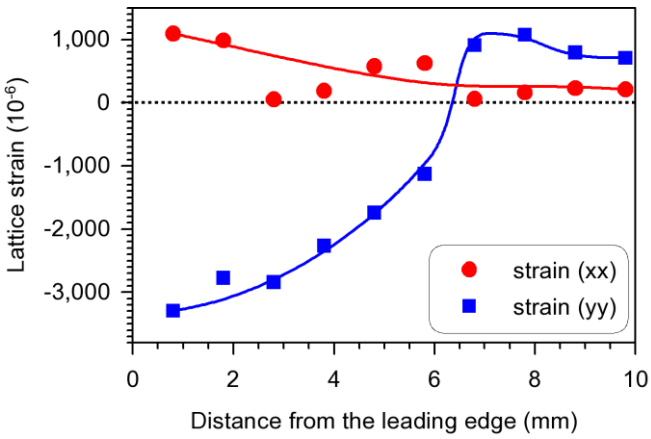

Figure 3: The residual strain distribution due to only LSP treatment as a function of distance from the L.E.

Figure 4(a) shows a 2D map of strain parallel to the L.E. for 0° FOD. It is evident that the FOD impact significantly alters the LSP induced initial compressive residual strains locally. Two observations can be made from this strain plot: (i) There is a large compressive strain region directly beneath the notch having a local maximum strain of -7000×10^{-6} and (ii) a small region of tensile strain is evident near the sides of the crater. Comparison with previous strain profiles around FOD damage in unpeened systems [6] suggests similar strain features but that LSP has biased the strain variations significantly towards compression. Figure 4b shows the residual strain distribution

for a 0° impact after a single block of combined LCF and HCF loading cycles (ratio of LCF and HCF = 1:1000; Outer Fiber Stress (OFS)=522MPa and R = 0.1and 0.7 for LCF and HCF, respectively). It is important to note that the two samples in Fig. 4a and b are different specimens. The damage in the sample represented in Figure 4b is 0.06 mm deeper than in the sample mapped for Figure 4a due to the scatter in the FOD impact process. The deeper damage depth resulted in larger compressive strain field at the bottom of the notch. It has been reported that, for Ti-6Al-4V, the applied stress needs to be 0.54 x σ_y (at R=0.1 and N=1 cycle) for strain relaxation to occur under fatigue loading conditions, whilst at 0.35 x σ_y, little relaxation was observed [7]. Even though the current test condition is about 0.56 x σ_y there is no evidence of relaxation after the fatigue cycles. The effect of fatigue loading might have been overshadowed by the different notch depths of the two samples. Figure 5 shows the residual elastic strains perpendicular to the leading edge measured post FOD (a) and post FOD and fatigue loading (b). Again, there seems no apparent evidence of strain relaxation after a block of 1000 HCF cycles on a LCF cycle, given the difference in the damage depths of the two samples.

For an unpeened edge, FOD introduced a large compressive stress at a distance 1.5 x crater radius away [1], whereas here large compressive strains appeared directly below the crater. Figure 6 shows the residual strain profiles around a 45° FOD impact. The damage depth is approximately half of the damage in 0° condition at 0.82 mm. Furthermore, the 45° impact created an asymmetric damage, a higher loss of material is observed in the entry side than the exit side. As our synchrotron X-ray measurements are averaged through the whole thickness any variation in the through thickness direction is not captured in the current study. Our recent results (unpublished) showed a significant through thickness strain variation for 45° FOD impact. The comparison of residual strain distribution between 0° and 45° crater suggest that the main difference is in the magnitude of the local maximum compressive strain, which is about -5000×10^{-6} in the case of 45° impact compared to -7000×10^{-6} for 0° impact. The variation in impact depths for the two samples might also contribute to the difference in the measured residual strains. It should also be noted that, unfortunately, we were unable to obtain reliable strain measurements within 0.8 mm of the LE for the 45° sample.

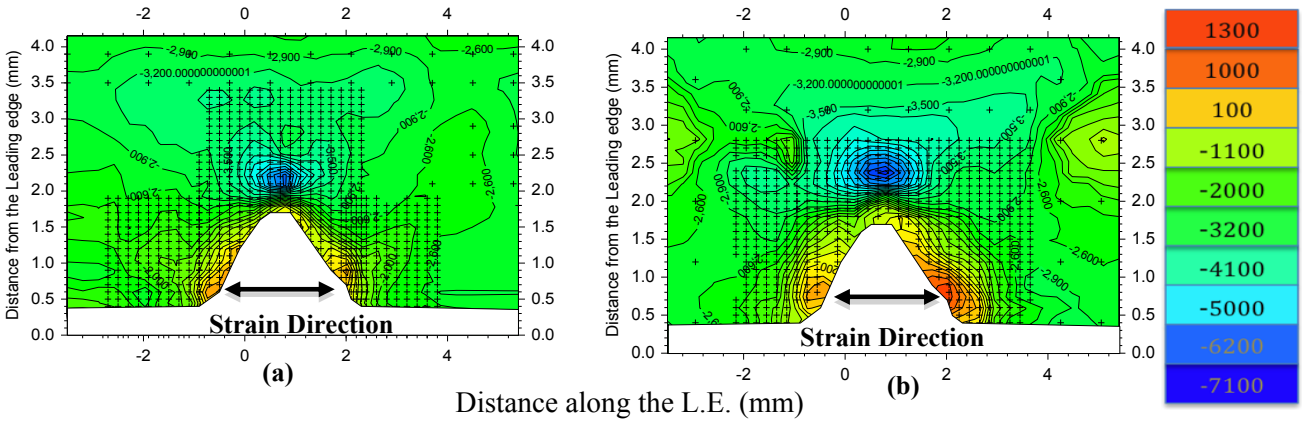

Figure 4: Residual elastic strain parallel to the leading edge: (a) After FOD to a damage depth of 1.49mm. (b) After FOD to a damage depth of 1.55mm followed by 1000 combined fatigue loading blocks (LCF:HCF=1:1000, S_{max}=435 MPa and R_{LCF} = 0.1and R_{HCF} =0.7).

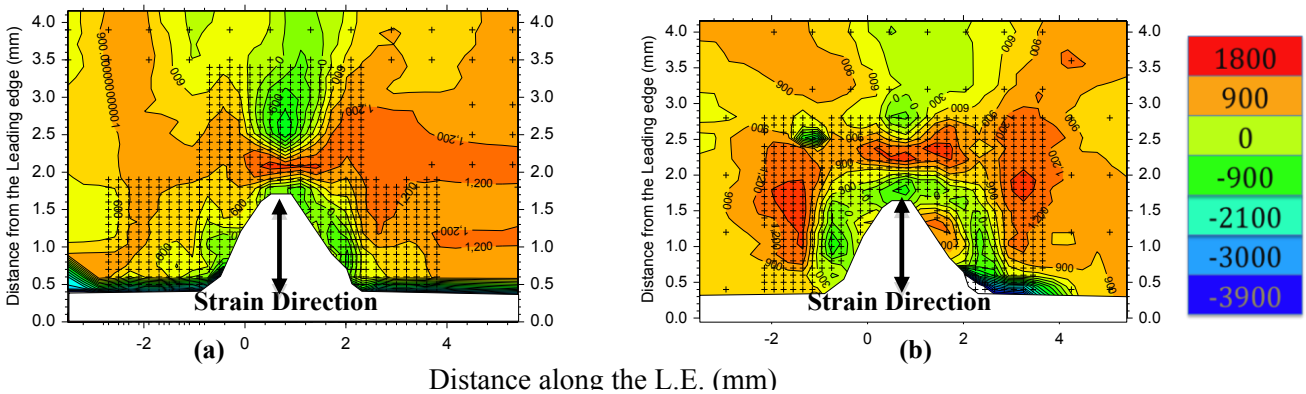

Figure 5: Residual elastic strains perpendicular to the leading edge: (a) After FOD to a damage depth of 1.49mm. (b) After FOD to a damage depth of 1.55mm followed by 1000 combined fatigue loading blocks (LCF:HCF=1:1000, S_{max}=435 MPa and R_{LCF} = 0.1and R_{HCF} =0.7).

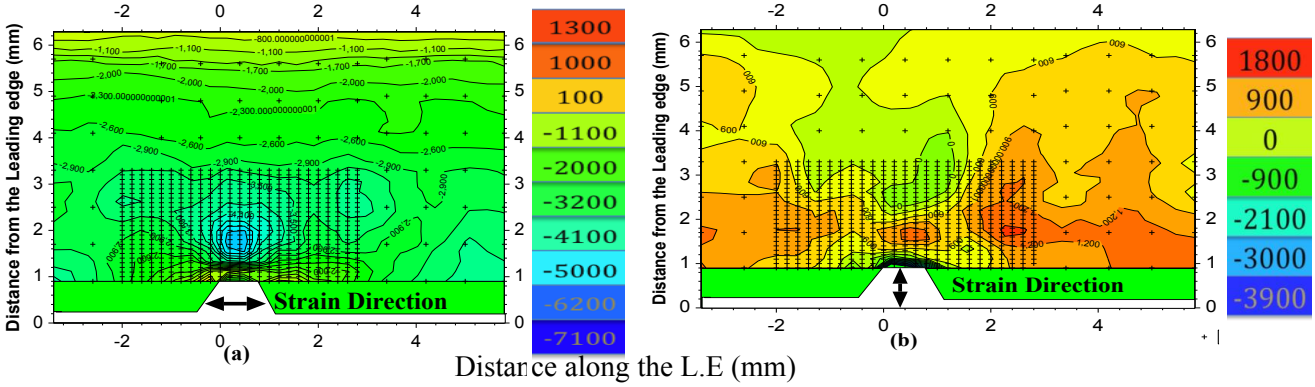

Figure 6: Residual elastic strains: a) Parallel and b) perpendicular to the L.E. around a 45° FOD impact to 0.82mm depth.

Conclusions

FOD impact introduces significant residual strains in the leading edge (L.E.) of aerofoil specimens. The laser peening successfully biases these towards compression such that a large compressive strain parallel to the L.E. was found just ahead of the notch. The 45° impact introduced less damage and thus lower residual strains than the 0° impact damage. There is no significant residual strain relaxation observed for the combined LCF and HCF fatigue loading condition examined.

Acknowledgements

The authors acknowledge Engineering and Physical Sciences Research Council (EPSRC) and the MOD Joint Grants Scheme for financial support and Rolls Royce plc for providing the materials, specimens and LSP treatment. The authors would like to thank the Advanced Photon Source (APS), Argonne National Laboratory, in Chicago, USA for provision of synchrotron X-ray radiation facilities and D.R. Haeffner and J D. Almer for experimental assistance during the experiment and Dr M. Winstone for support and helpful discussions.

References

[1] B. L. Boyce, X. Chen, J. W. Hutchinson, and R. O. Ritchie: *Mechanics of Materials*, Vol. 33 (8)(2001), p.441-454.

[2] P.J. Withers: Rep. Prog. Phys., Vol. 70 (2007), p. 2211–2264.

[3] G. Hammersley, L.A. Hackel, and F. Harris: *Optics and Lasers in Engineering,* Vol. 34 (2000), p. 327-337.

[4] R Hall, J Byrne, J Tong : *Fracture Fatigue Engng Mater Struct*., Vol. 31(2008), p.386-397.

[5] P. Frankel, PhD Thesis, The University of Manchester, UK (2008).

[6] P. Frankel, J. Ding, M. Preuss, J. Byrne, and P. J. Withers: Mat. Sci. Forum (ECRS7), Vol. 524-25(2006), p.291-296.

[7] B. L. Boyce, X. Chen, J. O. Peters, J. W. Hutchinson and R. O. Ritchie: Materials Science and Engineering A Vol. 349, Issues 1-2, (2003), p. 48-58

Materials Science Forum Vol. 652 (2010) pp 25-30

doi:10.4028/www.scientific.net/MSF.652.25

Determination of the Residual Stress Field around Scratches using Synchrotron X-rays and Nanoindentation

M. K. Khan[1,a], M. E. Fitzpatrick[1,b], S. V. Hainsworth[2,c], A. D. Evans[3,d], L. Edwards[1,4,e]

[1]Materials Engineering, The Open University, Walton Hall, Milton Keynes, MK7 6AA, UK
[2]Department of Engineering, University of Leicester, Leicester, LE1 7RH, UK
[3]Paul Scherrer Institut, CH-5232 Villigen PSI, Switzerland
[4]Currently at: ANSTO, PMB1, Menai, NSW 2234, Australia

[a]m.k.khan@open.ac.uk, [b]m.e.fitzpatrick@open.ac.uk, [c]svh2@leicester.ac.uk, [d]Alexander.Evans@psi.ch, [e]l.edwards@open.ac.uk

Keywords: Scratches, Residual stress, Synchrotron X-rays, Nanoindentation

Abstract

The residual strain field around scratches of 125 μm depth and 5 μm root radius have been measured using synchrotron X-ray diffraction. Scratches were produced using different tools in fine-grained aluminium alloy AA 5091. Residual stresses up to +1700 με were measured at the scratch tip, depending on the tool used to make the scratch.
The load-displacement curves obtained from nanoindentation were used to determine the residual stresses around the scratches. It was found that the load-displacement curves are sensitive to any local residual stress field present and behave according to the type of residual stresses. This combination of nanoindentation and synchrotron X-rays has been proved highly effective for the study of small-scale residual stresses around features such as scratches.

Introduction

Empirical understanding of fatigue crack growth from small defects is of tremendous importance and of significant concern for structural integrity of aerospace structures. During service, scratches can be accidentally created during maintenance operations. In principle the fatigue life for scratches is a function of the stress concentration around the root, which depends upon the depth and the root radius of the scratch, the associated microstructure, residual stress field, work hardening from plastic deformation during scratching, and relaxation or redistribution of these residual stresses in fatigue loading [6-8, 11-12]. Whilst several investigations have been done in the past to address the issues associated with stress concentration and microstructural distortion around small damage [1-2,4,6,8-10], a thorough understanding of the effect of residual stress around scratches is yet to be developed.
Unfortunately the ability to measure the local residual stress-strain fields around scratches is a difficult experimental problem in view of presence of the high stress gradients around the scratch root. To probe these local residual stress fields, experimental techniques are required that have a spatial resolution of the order of few microns. Synchrotron X-ray methods are well suited to the investigation of the residual stresses in the near-surface regions of engineered components [13]. High intensity and low divergence allows small gauge volumes to be defined in order to study stress fields existing over a range of tens or hundreds of microns.
In the past, there have not been many studies performed on the effect of submillimetre deep notches, gouges or scratches on fatigue life. Most of the research has been towards characterization of the effect of foreign object damage (FOD) on turbine engine blades in titanium alloys [3-12]. In almost every study the residual stresses have been cited as the most important factor in affecting the fatigue lives. Boyce *et al.* [11] measured the residual stress field around FOD using synchrotron X-

ray diffraction and found that the initial residual stress around the damage was highly tensile at 40% of the yield stress. They emphasized that the initial residual stress state can be substantially reduced by relaxation or redistribution during fatigue loading and may reduce by 30-50% of its initial value after the first fatigue cycle.
To successfully predict the fatigue lives of any foreign object damage, scratches, gouges etc., the residual stress field induced by the damage and relaxation of such residual stresses upon fatigue loading is an important parameter.
This paper presents investigation of the residual strain field around scratches in aluminium alloy 5091 induced by different tools, and validation of the results using nanoindentation. Residual strain fields were measured by synchrotron X-ray diffraction at the ID31 beam line of the European Synchrotron Radiation Facility (ESRF), Grenoble, France. This combination of nanoindentation and synchrotron X-rays is shown to have significant potential for the study of small-scale residual stresses around features such as scratches.

Materials, specimen and experimental details
Aluminium alloy 5091 was used in this study. Material properties are shown in Table 1 [16]. The average grain size was 0.6 µm. 5091 is a dispersion- and solution-strengthened alloy which contains a dispersion of very fine oxides (Al_2O_3) and carbides (Al_4C).

Material	Composition	Elastic Modulus (GPa)	Yield stress (MPa)	Poisson's ratio
AA 5091	Mg 4.0, Li 1.3 , C1 .1, O 0.4, Balance Aluminium	78	448	0.33

Table 1. Material properties of Aluminum alloy 5091

Specimen details
2-mm-thick plates were used. Two scratches of 125 µm depth and 5 µm root radius were produced in the 5091 with two different tools designated as tool A and B. Cross-sections of the scratches produced using these tools are shown in Fig. 1. For measurement with synchrotron X-rays a sample of 50 mm × 50 mm was cut from each sample with the scratch exactly at the centre of the sample.

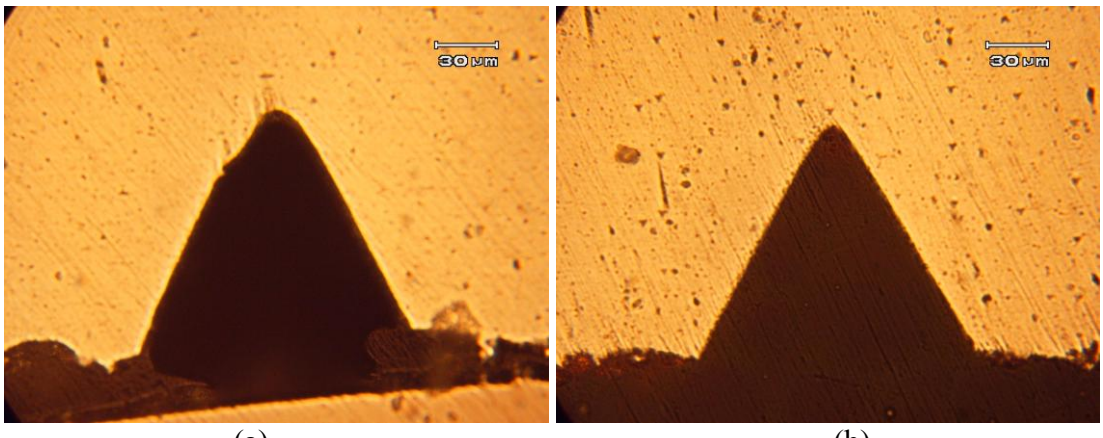

(a) (b)

Figure 1. Cross-section of scratches (a) Sample 1, Tool A (b) Sample 2, Tool B

The geometry of the components of the strains for the scratches is shown in Fig. 2(a). The coordinate system has been chosen with $x = y = z = 0$ at the scratch root tip at the centre of the sample. The x-direction was parallel to the crack propagating direction while the y-direction was perpendicular to the scratch plane and lay in the crack opening direction. The z-direction was parallel to the scratch length and this coordinate measured the depth from the scratch centre; z = 0